



The effect of the point spread function on sub-pixel mapping



Qunming Wang^a, Peter M. Atkinson^{a,b,c,*}

^a Lancaster Environment Centre, Lancaster University, Lancaster LA1 4YQ, UK

^b Geography and Environment, University of Southampton, Highfield, Southampton SO17 1BJ, UK

^c School of Geography, Archaeology and Palaeoecology, Queen's University Belfast, BT7 1NN, Northern Ireland, UK

ARTICLE INFO

Article history:

Received 20 November 2016

Received in revised form 24 February 2017

Accepted 4 March 2017

Available online xxxx

Keywords:

Land cover mapping

Downscaling

Sub-pixel mapping (SPM)

Super-resolution mapping

Point spread function (PSF)

Hopfield neural network (HNN)

ABSTRACT

Sub-pixel mapping (SPM) is a process for predicting spatially the land cover classes within mixed pixels. In existing SPM methods, the effect of point spread function (PSF) has seldom been considered. In this paper, a generic SPM method is developed to consider the PSF effect in SPM and, thereby, to increase prediction accuracy. We first demonstrate that the spectral unmixing predictions (i.e., coarse land cover proportions used as input for SPM) are a convolution of not only sub-pixels within the coarse pixel, but also sub-pixels from neighboring coarse pixels. Based on this finding, a new SPM method based on optimization is developed which recognizes the optimal solution as the one that when convolved with the PSF, is the same as the input coarse land cover proportion. Experimental results on three separate datasets show that the SPM accuracy can be increased by considering the PSF effect.

© 2017 Elsevier Inc. All rights reserved.

1. Introduction

Mixed pixels are inevitable in remote sensing images and have brought great challenges in land cover mapping. The spectral unmixing technique has been studied for decades to estimate the proportions of land cover classes within mixed pixels (Bioucas-Dias et al., 2012; Heinz and Chang, 2001; Keshava and Mustard, 2002). The proportions are at the same spatial resolution as the input images and cannot inform the spatial distribution of classes within mixed pixels. To further estimate the spatial distribution of land cover, sub-pixel mapping (SPM) was developed as a post-processing analysis of spectral unmixing outputs. SPM divides mixed pixels to sub-pixels and predicts their class attributes under the coherence constraint from prior spectral unmixing predictions (i.e., coarse land cover class proportions). SPM transforms the conventional pixel-level classification to a finer spatial resolution hard classification (Atkinson, 1997), which can provide more explicit thematic information (e.g., the boundaries between land cover classes can be characterized by more pixels).

In recent decades, various SPM approaches have been developed. As a post-processing step of spectral unmixing, two main groups of SPM approaches can be identified. The first group considers the relation between sub-pixels and solutions are always produced based on defined objectives. Based on the assumption of spatial dependence, the objective can be determined empirically as maximizing the spatial attraction between sub-pixels (Makido and Shortridge, 2007), maximizing the

Moran's I (Makido et al., 2007) or minimizing the perimeter of the area for each class (Villa et al., 2011). Based on prior knowledge, the objective can also be matching prior patterns extracted from training images, such as characterized by the semivariogram (Tatem et al., 2002), two-point histogram (Atkinson, 2008) or landscape structure (Lin et al., 2011). The SPM solutions of this type of methods are achieved based on optimization, including the Hopfield neural network (HNN) (Ling et al., 2010; Muad and Foody, 2012; Nguyen et al., 2011; Tatem et al., 2001), pixel swapping algorithm (PSA) (Atkinson, 2005; Shen et al., 2009; Xu and Huang, 2014), maximum a posteriori method (Zhong et al., 2015), genetic algorithm (Li et al., 2015; Mertens et al., 2003; Tong et al., 2016), and particle swarm optimization (PSO) (Wang et al., 2012). Several iterations are involved for this group of SPM methods and, thus, a relatively long computing time may be required. The second group of SPM methods considers the relation between sub-pixels and neighboring pixels. The coarse class proportions within each pixel are used directly to characterize the relation between it and sub-pixels and calculate the fine spatial resolution proportions for sub-pixels. Under the coherence constraint, the sub-pixel classes are determined by comparing the fine spatial resolution proportions. As the coarse proportions are fixed for a given pixel, iterations (as in the first method type) are not necessarily involved and SPM solutions can be produced more quickly. Methods falling into this type include sub-pixel/pixel spatial attraction model (SPSAM) (Mahmood et al., 2013; Mertens et al., 2006; Xu et al., 2014), back-propagation neural network-based algorithm (Gu et al., 2008; Zhang et al., 2008), learning-based algorithm (Zhang et al., 2014), kriging (Verhoeve and Wulf, 2002; Boucher and Kyriakidis, 2006) and radial basis function

* Corresponding author.

E-mail address: pma@lancaster.ac.uk (P.M. Atkinson).

(RBF) (Wang et al., 2014a) interpolation. They can also be summarized as the soft-then-hard SPM (STHSPM) algorithms, a concept proposed in our previous work (Wang et al., 2014b; Chen et al., 2015). In addition, to reduce the uncertainty introduced by spectral unmixing, some SPM methods that do not rely absolutely on coarse proportions were developed, including spatial-spectral methods (Ardila et al., 2011; Kasetkasem et al., 2005; Li et al., 2014; Tolpekin and Stein, 2009), spatial regularization (Ling et al., 2014; Zhang et al., 2015) and contouring methods (Foody and Doan, 2007; Ge et al., 2014; Su et al., 2012).

In remote sensing images, the point spread function (PSF) effect exists ubiquitously. It means that the signal for a given pixel is a weighted combination of contributions from within the pixel and also contributions from neighboring pixels (Townshend et al., 2000; Van der Meer, 2012). The PSF can brighten dark objects and darken bright objects observed from the surface (Huang et al., 2002). It results in a fundamental limit on the amount of information that remote sensing images can contain (Manslow and Nixon, 2002). The PSF is a two-dimensional function accounting for both the across-track and along-track directions (Campagnolo and Montano, 2014; Radoux et al., 2016). The PSF effect is caused mainly by the optics of the instrument, the detector and electronics, atmospheric effects, and image resampling (Huang et al., 2002; Schowengerdt, 1997).

The PSF effect may not be an important issue for homogeneous regions, but it is crucial for heterogeneous landscapes dominated by mixed pixels. To the best of our knowledge, very few SPM methods have considered the PSF effect in downscaling. For example, in most of the existing SPM methods, the coherence constraint from class proportions is satisfied simply by fixing the number of sub-pixels for each class within a single coarse pixel (i.e., the ideal square wave PSF is considered). The number of sub-pixels to be allocated to a class within a coarse pixel is calculated as the product of the coarse class proportion within the coarse pixel and the square of the zoom factor. Due to the PSF effect, however, the coarse proportions estimated by spectral unmixing are actually a function, in part, of the neighboring coarse pixels. The uncertainty in coarse proportions is propagated to the post-SPM process where the coarse proportions contaminated by neighboring coarse pixels are used as the coherence constraint. There is, therefore, a great need for an approach accounting for the PSF effect in SPM to increase the prediction accuracy.

There are two plausible solutions to cope with the PSF effect in SPM. One is to consider the PSF effect in the pre-spectral unmixing process and to estimate more reliable coarse proportions from observed multi-spectral images. Based on the more reliable predictions, the PSF need not be considered in SPM (i.e., the ideal square wave PSF can be considered in SPM, as in existing SPM approaches). However, spectral unmixing is an ill-posed inverse problem. It is more complicated when part of the neighboring coarse pixels (i.e., neighboring sub-pixels) are involved as this technique is generally performed at the pixel resolution. Currently, it is challenging to account for the PSF in spectral unmixing and obtain reliable proportions. The alternative solution, considered here, is to model the PSF effect in the SPM process, based on the proportions contaminated by neighboring coarse pixels. This strategy is more feasible as SPM is conducted at the sub-pixel scale and contributions from neighboring sub-pixels in PSF can be straightforwardly modeled.

In this paper, to increase the SPM accuracy, the PSF effect is considered directly in the SPM process. Most SPM methods need to first calculate the number of sub-pixels for each class within each coarse pixel. Based on these fixed numbers, the sub-pixel classes are then predicted. This is not a problem for the ideal square wave PSF, as mentioned earlier. When considering the non-ideal PSF, however, the coarse proportions are a convolution of the sub-pixel class values in a larger local window, rather than the single coarse pixel in the ideal square-wave PSF. In this case, the number of sub-pixels for each class in each coarse pixel cannot be determined using only the single coarse proportion (i.e., product of the coarse proportion and the square of the zoom factor,

as in existing SPM methods), and it actually cannot be calculated explicitly. In this case, SPM methods such as the STHSPM algorithms are not suitable choices. A plausible solution to this issue is to convolve the fine spatial resolution SPM realization with the PSF and compare the estimated proportion with the actual coarse proportion, and use the error to guide further updating of the current realization. The iteration-based HNN is a method of this type. Therefore, in this paper, the HNN is used to reduce the uncertainty in SPM introduced by the PSF effect.

The remainder of this paper is organized into four sections. Section 2 first introduces the mechanism of the PSF effect in SPM and then the details of the proposed strategy for considering the PSF in SPM. The experimental results for three groups of datasets are provided in Section 3 for validation of the proposed method. Section 4 further discusses the proposed SPM method, followed by a conclusion in Section 5.

2. Methods

2.1. The PSF effect in SPM

This section will illustrate the PSF effect in SPM and demonstrate that the coarse proportions in SPM are a convolution of the sub-pixel class values in a local window centered at the coarse pixel. Let \mathbf{S}_V be the spectrum of coarse pixel V , \mathbf{R}_k be the spectrum of class endmember k ($k = 1, 2, \dots, K$, where K is the number of land cover classes), and $F_k(V)$ be the proportion of class k in pixel V . Based on the classical linear spectral mixture model (Bioucas-Dias et al., 2012; Heinz and Chang, 2001; Keshava and Mustard, 2002), the spectrum of each coarse pixel is a linear combination of the spectrum of endmembers, where the weights are determined as the class proportions within the coarse pixel. That is

$$\mathbf{S}_V = \sum_{k=1}^K \mathbf{R}_k F_k(V) \quad (1)$$

Due to the PSF effect in remote sensing images, Eq. (2) holds

$$\mathbf{S}_V = \mathbf{S}_v * h_v \quad (2)$$

where \mathbf{S}_v is the spectrum of sub-pixel v , h_v is the PSF and $*$ is the convolution operator. For sub-pixel v , its spectrum \mathbf{S}_v can be characterized as

$$\mathbf{S}_v = \sum_{k=1}^K \mathbf{R}_k I_k(v) \quad (3)$$

in which $I_k(v)$ is a class indicator as follows

$$I_k(v) = \begin{cases} 1, & \text{if sub-pixel } v \text{ belongs to class } k \\ 0, & \text{otherwise} \end{cases} \quad (4)$$

By substituting Eq. (3) into Eq. (2), we have

$$\mathbf{S}_V = \left[\sum_{k=1}^K \mathbf{R}_k I_k(v) \right] * h_v = \sum_{k=1}^K \mathbf{R}_k [I_k(v) * h_v] \quad (5)$$

The comparison between Eqs. (1) and (5) leads to

$$F_k(V) = I_k(v) * h_v \quad (6)$$

Let z be the zoom factor, that is, each coarse pixel is divided into z by z sub-pixels. As shown in the one dimensional illustration in Fig. 1, when the PSF takes the ideal square wave filter in Eq. (7)

$$h_v(i, j) = \begin{cases} \frac{1}{z^2}, & \text{if } (i, j) \in V(i, j) \\ 0, & \text{otherwise} \end{cases} \quad (7)$$

where (i, j) is the spatial location of the sub-pixel and $V(i, j)$ is the spatial extent of the coarse pixel V containing the sub-pixel at (i, j) . Further, the

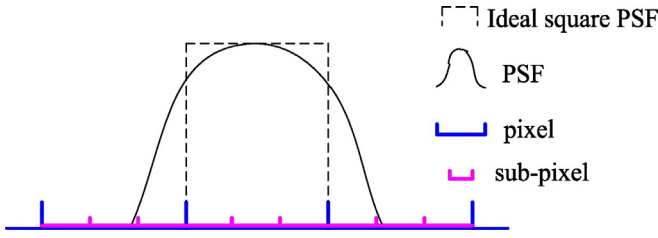


Fig. 1. A one dimensional illustration of the PSF in SPM. Based on the real PSF, the coarse pixel value (or coarse class proportion) should be a convolution of the sub-pixel values (or sub-pixel class indicators) located within the local window centered at the coarse pixel, rather than only within the single coarse pixel (as assumed in the ideal square wave PSF).

convolution in Eq. (6) can be simplified as

$$F_k(V) = \frac{\sum_{i,j=1}^z I_k(v_{ij})}{z^2} \quad (8)$$

In Eq. (8), all sub-pixels v_{ij} are located within coarse pixel V . This means that based on the assumption of an ideal square wave PSF, the coarse class proportion estimated from the linear spectral mixture model in Eq. (1) is viewed as the average of all sub-pixel class indicators within the pixel. This is the common case considered in most SPM methods.

In reality, the PSF is different to the ideal square wave filter. The spatial coverage of h_V is generally larger than a coarse pixel size, but is finite, as shown in Fig. 1. For example, the PSF can be the Gaussian filter, which is used widely in remote sensing (Campagnolo and Montano, 2014; Huang et al., 2002; Manslow and Nixon, 2002; Townshend et al., 2000; Van der Meer, 2012; Wenny et al., 2015)

$$h_V(i, j) = \begin{cases} \frac{1}{2\pi\sigma^2} \exp\left[-\left(\frac{i^2 + j^2}{2\sigma^2}\right)\right], & \text{if } (i, j) \in V'(i, j) \\ 0, & \text{otherwise} \end{cases} \quad (9)$$

where σ is the standard deviation (width of the Gaussian PSF) and $V'(i, j)$ is the spatial extent of the local window centered at coarse pixel V (V covers the sub-pixel at (i, j)), see Fig. 1. Thus, any sub-pixel v involved in the calculations in Eqs. (2) and (6) falls within a wider spatial coverage $V'(i, j)$, rather than only within $V(i, j)$. This means that based on the linear spectral mixture model in Eq. (1), the estimated coarse class proportions within each coarse pixel are actually a convolution of the sub-pixels in the local window centered at the coarse pixel, rather than only the sub-pixels within the coarse pixel (i.e., not the case in Eq. (8)).

2.2. Enhancing SPM by considering the PSF effect

In conventional SPM, the number of sub-pixels for each class needs to be determined in advance, which is used as a coherence constraint in the mapping process. Let $N_k(V)$ be the number of sub-pixels for class k in pixel V , which is usually calculated as

$$N_k(V) = \text{round}[F_k(V) \times z^2] \quad (10)$$

Table 1

Accuracy of the coarse proportion images for the six targets.

	T1	T2	T3	T4	T5	T6
RMSE	0.0421	0.0602	0.0671	0.0707	0.0924	0.0972
CC	0.9949	0.9902	0.9820	0.9868	0.9677	0.9668

From Section 2.1, it is concluded that in reality the estimated coarse proportions are contaminated by their neighboring pixels due to the PSF effect (see Eq. (6)). Therefore, it is generally incorrect to use Eq. (10) for the coherence constraint in SPM, unless the correct land cover proportions (i.e., not contaminated by neighbors) can be produced. As can be seen from Eq. (5), even when the endmember set R_k and PSF h_V are known perfectly, it is not trivial to determine the correct proportions. This is because the coarse proportions can sometimes be functions of neighboring sub-pixels, as can be seen from Eq. (6) and Fig. 1. In this case where sub-pixels are involved, spectral unmixing becomes challenging, as unmixing is carried out at the pixel resolution and cannot account for proportions at the sub-pixel resolution. Townshend et al. (2000) and Huang et al. (2002) proposed an interesting deconvolution method to reduce the impact of the PSF in coarse proportion predictions. This method was developed at the pixel resolution, which quantifies the contributions from neighbors in units of coarse pixels. That is, it treats all sub-pixels in a surrounding coarse pixel equally and assumes a uniform contribution to the center coarse pixel. According to Fig. 1, however, sub-pixels in the surrounding coarse pixel have a different spatial distance to the center coarse pixel and thus, should have different contributions to the center coarse proportion (e.g., some sub-pixels even have no contribution).

In this paper, the coarse proportions contaminated by pixel neighbors are directly considered in SPM. As $N_k(V)$ cannot be calculated explicitly, conventional SPM methods such as the STHSPM algorithms cannot be used. Guided by the mechanism in Eq. (6), the ideal SPM solution should be the one that when convolved with the PSF, is the same as the coarse proportion. Alternatively, an optimization-based SPM method is employed in this paper, where the convolution of the current SPM realization is compared with the contaminated coarse proportions for updating SPM predictions iteratively. The HNN is a method suitable for this task and is used for accounting for the PSF in SPM. The HNN has been used widely in SPM, appreciating its highly satisfactory performance (Ling et al., 2010; Muad and Foody, 2012; Nguyen et al., 2011; Tatem et al., 2001). It considers each sub-pixel as a neuron and works by minimizing an energy function composed of a goal and a coherence constraint term. The HNN accounting for the PSF effect is introduced below.

Suppose (k, i, j) is a neuron for sub-pixel at location (i, j) and is on the network layer representing land cover class k , and q_{kij} is its output. If q_{kij} is 1, it means that the sub-pixel at (i, j) is belongs to class k , and if q_{kij} is 0, the sub-pixel does not belong to class k . Using the HNN, the outputs are update iteratively for each sub-pixel. The output q_{kij} is a function of the input signal u_{kij}

$$q_{kij} = \frac{1}{2} [1 + \tanh(\lambda u_{kij})] \quad (11)$$

where λ determines the steepness of the function. The input u_{kij} for the t -th iteration is updated by

$$u_{kij}(t + dt) = u_{kij} + \frac{du_{kij}(t)}{dt} dt \quad (12)$$

in which dt is a time step. The second term on the right hand side of Eq. (12) is the energy change of the neuron and is described as

$$\frac{du_{kij}(t)}{dt} = -\frac{dE_{kij}}{dq_{kij}} \quad (13)$$

In Eq. (13), E represents the network energy function and is described as

$$E = \sum_k \sum_i \sum_j (w_1 G1_{kij} + w_2 G2_{kij} + w_3 P_{kij} + w_4 M_{kij}) \quad (14)$$

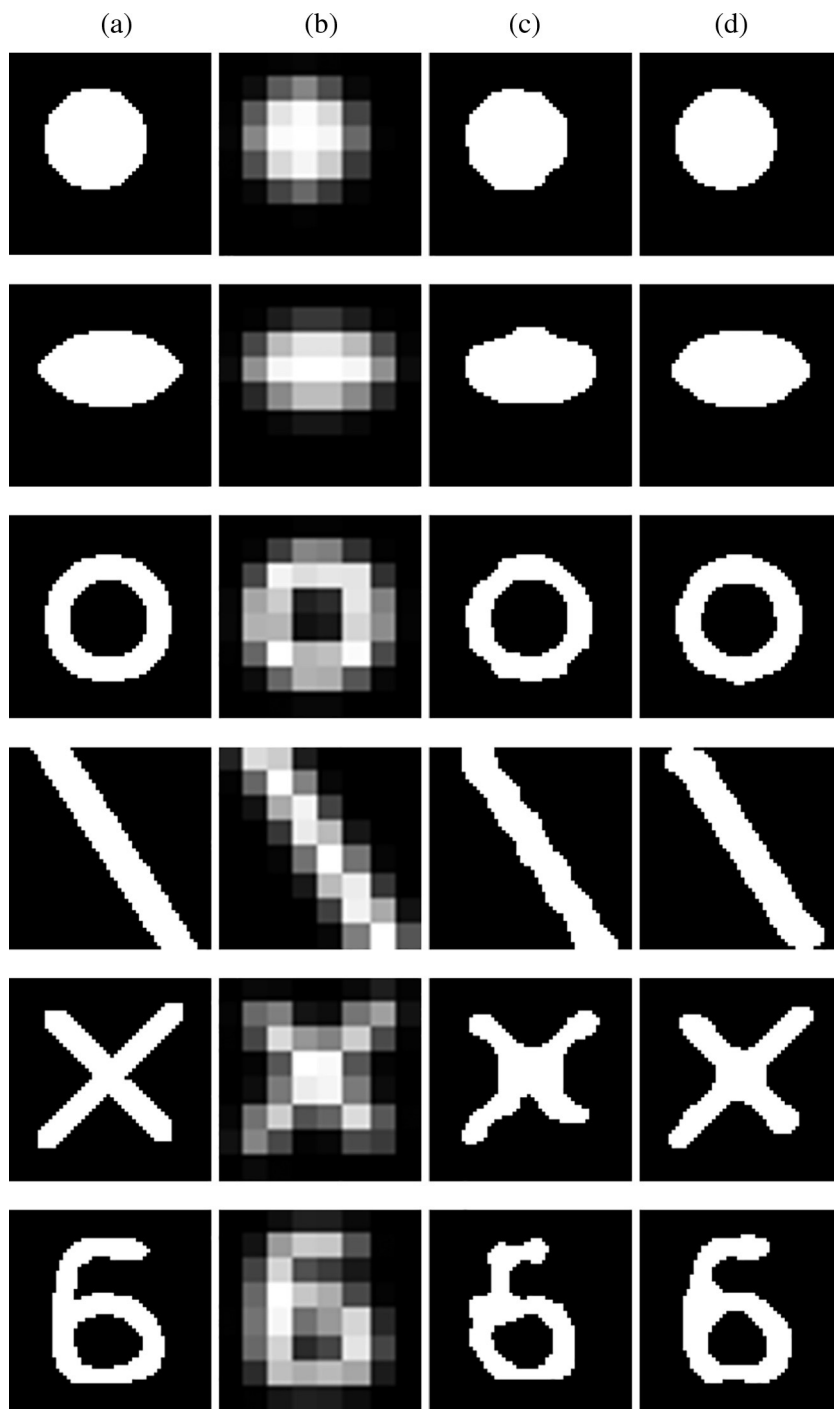


Fig. 2. SPM results of six targets. (a) Reference images (56 by 56 pixels). (b) Coarse images (8 by 8 pixels) produced by degrading (a) with a Gaussian PSF and a factor of 7. (c) SPM results produced using the HNN without PSF (or with ideal PSF). (d) SPM results produced using the proposed HNN with the Gaussian PSF. Lines 1–6 are results for T1–T6.

where w_1 , w_2 , w_3 and w_4 are four weights, $G1$ and $G2$ are two spatial clustering functions characterizing spatial dependence, P is the proportion constraint and M is the multi-class constraint (Ling

et al., 2010; Nguyen et al., 2011). Accordingly, the energy change of the neuron for sub-pixel at (i, j) in Eq. (13) is determined by

$$\frac{dE_{kij}}{dq_{kij}} = w_1 \frac{dG1_{kij}}{dq_{kij}} + w_2 \frac{dG2_{kij}}{dq_{kij}} + w_3 \frac{dP_{kij}}{dq_{kij}} + w_4 \frac{dM_{kij}}{dq_{kij}} \quad (15)$$

Table 2
OA (%) of HNN-based SPM with two different schemes for the six binary images.

		T1	T2	T3	T4	T5	T6
$z = 4$	No PSF	99.34	98.72	98.00	98.44	98.30	96.66
	PSF	99.34	99.52	99.26	99.19	98.67	98.08
	RRE	0%	62.50%	63.00%	48.08%	21.76%	42.51%
$z = 7$	No PSF	99.41	97.31	97.89	97.34	94.48	90.53
	PSF	99.46	99.26	98.16	97.91	97.51	95.18
	RRE	8.47%	72.49%	12.80%	21.43%	54.89%	49.10%

Table 3
Accuracy of the coarse proportion images for the land cover map.

	Roads	Trees	Buildings	Grass	Mean
RMSE	0.0440	0.0576	0.0591	0.0924	0.0633
CC	0.9866	0.9867	0.9844	0.9792	0.9842

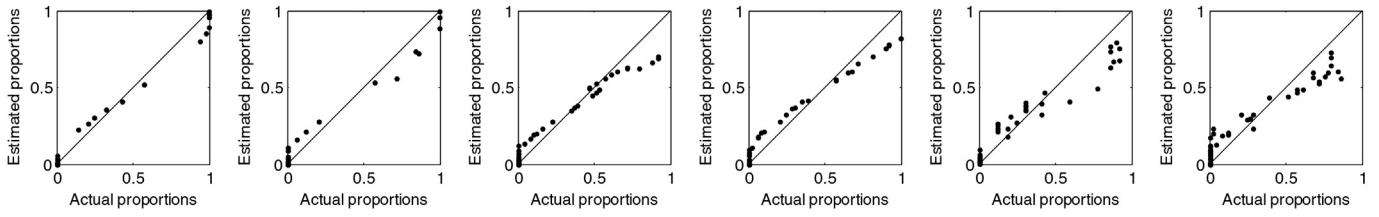


Fig. 3. Relation between the actual proportions (for white target) and proportions (for white target) contaminated due to the PSF effect for the six binary images ($z = 7$). From left to right are results for T1–T6.

The first two terms of the right hand side of Eq. (15) are calculated as

$$\frac{dG1_{kij}}{dq_{kij}} = \frac{1}{2} \left[1 + \tanh \left(\frac{1}{8} \left(\sum_{b=i-1}^{i+1} \sum_{c=j-1}^{j+1} q_{kbc} - q_{kij} \right) - 0.5 \right) \lambda \right] (q_{kij} - 1) \quad (16)$$

$$\frac{dG2_{kij}}{dq_{kij}} = \frac{1}{2} \left[1 - \tanh \left(\frac{1}{8} \left(\sum_{b=i-1}^{i+1} \sum_{c=j-1}^{j+1} q_{kbc} - q_{kij} \right) - 0.5 \right) \lambda \right] q_{kij} \quad (17)$$

If the average output of the surrounding neurons is larger than 0.5, the function G1 increases the neuron output to approach 1 to increase the spatial correlation between neighboring sub-pixels. Otherwise, if the average output of the surrounding neurons is less than 0.5, the function G2 decreases the neuron output to 0.

The multi-class constraint means that for any sub-pixel, the sum of neuron outputs for all K classes should be equal to 1, thus

$$\frac{dM_{kij}}{dq_{kij}} = \left(\sum_{n=1}^K q_{nij} \right) - 1 \quad (18)$$

Considering the PSF effect, the proportion constraint for class k is expressed as

$$\frac{dP_{kij}}{dq_{kij}} = L_k(V_{ij}) - F_k(V_{ij}) \quad (19)$$

where V_{ij} is the coarse pixel that sub-pixel at (i, j) falls within, $F_k(V_{ij})$ is the target coarse proportion of class k in the pixel (i.e., spectral unmixing predictions), and $L_k(V_{ij})$ is the coarse proportion estimated as convolution of the current SPM realization. Based on the mechanism in Eq. (6), $L_k(V_{ij})$ is calculated as

$$L_k(V_{ij}) = \frac{1}{2} [1 + \tanh(q_k - 0.5)\lambda] h_V \quad (20)$$

$$= \iint_{(x,y) \in V'(i,j)} \frac{1}{2} [1 + \tanh(q_k - 0.5)\lambda] h_V(x - i_0, y - j_0) dx dy$$

in which $V'(i, j)$ is defined in the same way as that in Eq. (9) and (i_0, j_0) is the spatial location of the center of coarse pixel V_{ij} . The tanh function is

Table 4
SPM accuracy (%) of the different SPM schemes for the experiment on the land cover map.

		SPSAM (no PSF)	RBF (no PSF)	PSA (no PSF)	HNN (no PSF)	HNN (PSF)
$z = 4$	Roads	94.59	94.64	93.81	98.92	99.78
	Trees	92.16	92.53	91.45	94.38	95.41
	Buildings	91.20	91.69	90.43	93.50	95.28
	Grass	93.82	94.10	93.22	97.86	98.57
	OA	93.17	93.47	92.50	96.62	97.58
	RRE (in OA)	64.57%	62.94%	67.73%	28.40%	
$z = 8$	Roads	88.24	88.86	87.26	95.13	98.03
	Trees	86.20	87.48	86.13	85.20	90.08
	Buildings	82.51	83.81	81.83	82.92	88.64
	Grass	91.77	90.98	91.74	95.97	95.85
	OA	89.42	89.15	89.23	92.15	94.00
	RRE (in OA)	43.29%	44.70%	44.29%	23.57%	

used in Eq. (20) to ensure that if the neuron output q_k is above 0.5, it is counted as an output of 1 (i.e., belongs to class k) for the coarse proportion calculation; If q_k is below 0.5, it is not counted for class k instead. This ensures that the neuron output exceeds 0.5 in order to be counted within the calculations for each class.

In Eq. (19), the target coarse proportion $F_k(V_{ij})$ is used to examine the current SPM realization. The convolution of the final SPM prediction should be the same as the target coarse proportion. Specifically, if the convolution of the current SPM realization, $L_k(V_{ij})$, is larger than the target proportion $F_k(V_{ij})$, a positive gradient is produced and the energy is reduced to decrease the neuron output (see Eqs. (12) and (13)) to cope with this overestimation issue. On the contrary, if $L_k(V_{ij})$ is smaller than $F_k(V_{ij})$, a negative gradient is produced and the neuron output is increased correspondingly to cope with underestimation. After a number of iterations (usually over 1000), $L_k(V_{ij})$ will approach $F_k(V_{ij})$, suggesting that the convolution of the final prediction is almost identical to the target coarse proportion contaminated by the PSF effect. In this way, the PSF effect in SPM is considered and a more reliable sub-pixel class distribution can be reproduced. It should be noted that the proposed HNN-based SPM method accounting for the PSF is suitable for any PSF. Its implementation is not affected by the specific form of PSF. Once the PSF of the sensor is available or estimated, it can be used readily in the proposed method, as shown in Eq. (20).

As suggested in Tatem et al. (2001), for the HNN, the network will converge to similar energy minima given any initialization and the network will converge to an accurate prediction in fewer iterations if a proportion-constrained initialization is used. This scheme was employed in the proposed method for faster convergence of the optimization. According to Eq. (6), in the estimated coarse proportions images, if a pixel is presented as a pure pixel (e.g., belongs entirely to class k), all sub-pixels in the local window centered at the coarse pixel must belong to class k . Thus, for any pure pixel in the coarse proportion image for class k , we directly initialize the neuron outputs of all sub-pixels within it as 1 for class k and 0 for other classes. These values are fixed and not changed in the optimization process. For mixed pixels, random initialization (between 0 and 1) was applied.

3. Experiments

Experiments were carried out on three groups of synthetic datasets, including a dataset with six different targets, a land cover map with multiple classes, and a multispectral image. They were used to test the performance of SPM methods on different typical shapes in Section 3.1, multiple classes in Section 3.2 and the case involving realistic unmixing in Section 3.3. As mentioned earlier, the proposed method is suitable for any PSF. The estimation of the PSF of sensors is still an

Table 5
Accuracy of the coarse proportion images for the multispectral image.

		C1	C2	C3	C4	Mean
Actual proportion	RMSE	0.0873	0.0950	0.0517	0.0529	0.0717
	CC	0.9703	0.9766	0.9844	0.9692	0.9751
Convolved proportion	RMSE	0.0418	0.0303	0.0085	0.0206	0.0253
	CC	0.9885	0.9957	0.9992	0.9913	0.9937

Table 6

SPM accuracy (%) of the different SPM schemes for the experiment on the multispectral image.

	SPSAM (no PSF)	RBF (no PSF)	PSA (no PSF)	HNN (no PSF)	HNN (PSF)
C1	75.88	77.65	75.98	76.89	81.40
C2	90.92	91.71	90.92	96.57	96.26
C3	82.50	84.30	81.68	87.08	89.81
C4	71.18	73.38	72.95	77.75	83.15
OA	85.91	87.07	85.95	90.57	91.86
RRE (in OA)	42.23%	37.05%	42.06%	13.68%	

open problem, and uncertainty unavoidably exists in the process. It is beyond the scope of this paper to estimate the PSF. Alternatively, to concentrate solely on the performance of SPM, all coarse data for the three groups of datasets were produced by convolving the available fine spatial resolution data, using a Gaussian PSF shown in Eq. (9), which is a widely used PSF (Campagnolo and Montano, 2014; Huang et al., 2002; Manslow and Nixon, 2002; Townshend et al., 2000; Van der Meer, 2012; Wenny et al., 2015). The width of the PSF was set to half of the coarse pixel size. Based on this strategy, the fine spatial resolution data are known perfectly and can be used as a reference for evaluation. All SPM results were evaluated both visually and quantitatively. For quantitative evaluation, the classification accuracy of each class and the overall accuracy (OA) in terms of the percentage of correctly classified pixels were used. In addition, to emphasize the improvement of the proposed method over the other methods, an index called the reduction in remaining error (RRE) (Wang et al., 2015) was also used, as calculated below

$$\text{RRE} = \frac{\text{RE}_1 - \text{RE}_0}{\text{RE}_1} \times 100\% \quad (21)$$

where RE_1 and RE_0 are the remaining errors of OA (i.e., $100\% - \text{OA}$) for the benchmark method and the proposed method, respectively.

3.1. Experiment on the six targets

In this experiment, six binary images (pixel value 1 for white target while 0 for black background) with different targets were used for validation. They represent typical, basic shapes in nature. All six images have a spatial size of 56 by 56 pixels and were marked as T1–T6, as shown in Fig. 1(a). Each image was degraded with a Gaussian PSF and a zoom factor of 7, generating coarse images with 8 by 8 pixels, as shown in Fig. 1(b). The coarse images are exactly the simulated coarse proportions of the white targets in each image.

Fig. 3 shows the relation between the PSF-convolved coarse proportions and actual proportions for the six white targets. The actual

proportions were generated by averaging the sub-pixel class indicators within each coarse pixel. As observed from the plots, the proportions are very different to the actual values due to the PSF effect. For example, in all six plots, many proportions should be 0 (i.e., pure background pixel and no target pixel in the coarse pixel), but were actually calculated as values larger than 0 (i.e., mixed pixel). The reason is that although no target pixels exist in a coarse pixel, they may be located in neighboring pixels. According to Eq. (6), these neighboring pixels will contaminate the center pixel which will then not be recognized as a pure background pixel. The accuracies of the coarse proportions were quantified in terms of root mean square error (RMSE) and correlation coefficient (CC), as listed in Table 1. The uncertainty in the PSF-convolved coarse proportions motivates the development of SPM methods considering the PSF effect.

The SPM results of the HNN without PSF (that is, with ideal PSF) and with the Gaussian PSF are shown in Fig. 2(c) and Fig. 2(d), respectively. It is seen clearly that by considering the PSF effect, more accurate SPM results can be produced. In the results for target T1–T3, the proposed method produces more compact shapes that are closer to the reference. For T4 and T5, the proposed method produces a straighter line than the HNN without PSF. In T6, the more complex boundaries of the target are reproduced by the proposed method.

Quantitative assessment in terms of OA (accuracy statistics for both target and background in each image) is listed in Table 2. As mentioned earlier, for pure pixels, all sub-pixels within them are simply assigned to the same class to which the pure pixel belongs. As suggested by the existing literature (Mertens et al., 2003), this copy process will only increase the SPM accuracy statistics without providing any useful information on the actual performance of the SPM methods. Hence, for the synthetic coarse images, we did not consider the pure pixels in the accuracy statistics. The quantitative evaluation was conducted for two different zoom factors, $z = 4$ and 7 . As observed from the table, the HNN with PSF produces a larger OA than the HNN without PSF. Moreover, the advantage tends to be more obvious when a larger zoom factor is involved. More precisely, for T2 and T5, using the proposed method, the accuracy gains are below 1% for $z = 4$, but increase to be above 2% for $z = 7$. For T6, the proposed method considering the PSF increases the OA by 1.4% for $z = 4$ and 4.7% for $z = 7$. In addition, all RREs are generally large (over 10%) and some even reach over 60%, suggesting that the accuracy increase is obvious.

The influence of the width of the Gaussian PSF was also analyzed, as shown in Fig. 4. The fine spatial resolution T1, T2 and T5 images were degraded with a factor of 7. Three PSF sizes, 0.5, 0.75 and 1 coarse pixels, were considered for each target. Three observations can be made from the results in Fig. 4. First, for all PSF sizes, the consideration of the PSF effect can lead to consistently larger OA than that produced without the PSF. Second, the accuracy of SPM methods decreases as the width of the PSF increases, no matter whether the PSF is accounted for or not.

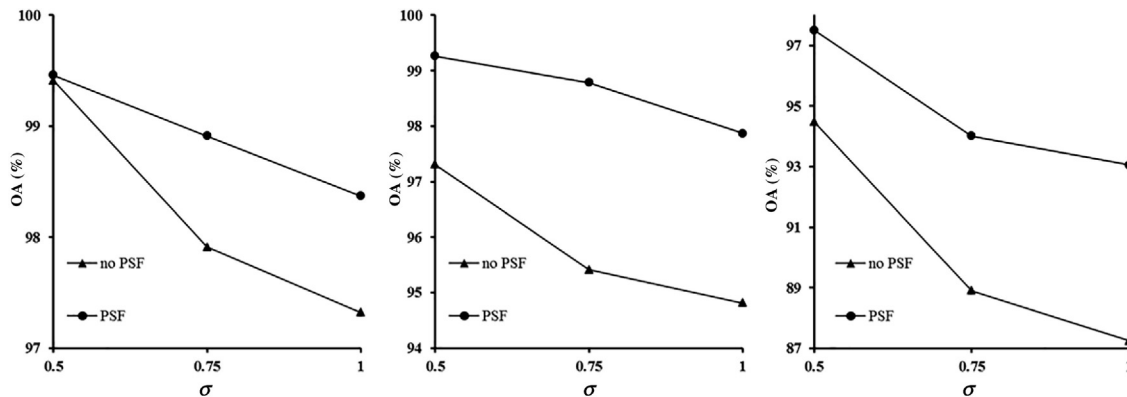


Fig. 4. The accuracy of the two SPM methods in relation to the width of the PSF (in units of coarse pixel, which was produced by degrading Fig. 2(a) with a factor of 7). From left to right are results for T1, T2 and T5, respectively.

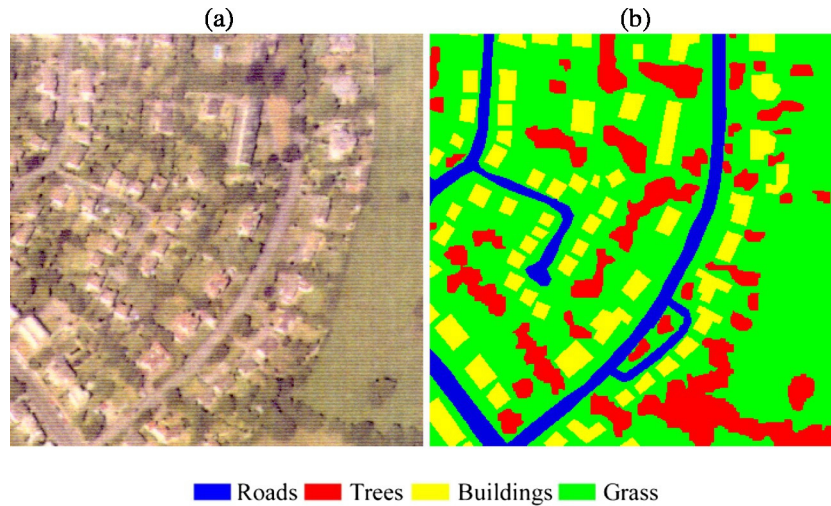


Fig. 5. The land cover map. (a) Original aerial photograph. (b) Reference map drawn manually from (a).

This is because more neighboring sub-pixels are involved in the convolution process and the SPM problem becomes more complex as the width increases. Third, as the width increases, the advantage of considering the PSF is more obvious.

3.2. Experiment on the land cover map with multiple classes

A land cover map produced from an aerial photograph covering an area in Bath, UK was used in this experiment, as shown in Fig. 5. The image has a spatial resolution of 0.6 m, and a spatial size of 360 by 360 pixels. Four classes were identified in the land cover map, including roads, trees, buildings and grass. The map was degraded with a factor of 8 and a Gaussian PSF, generating four proportion images at a spatial resolution of 4.8 m. The relation between the simulated coarse proportions and actual proportions is shown in the plots in Fig. 6. Table 3 lists the accuracies of the proportions. Similarly to the observation in Fig. 3 and Table 1, the two types of proportions are very different due to the PSF effect.

The proposed method is not only compared to the original HNN method, but also to several typical SPM methods. As mentioned in the Introduction, there are mainly two families of SPM methods for post-processing of spectral unmixing. One is the method considering the relation between sub-pixels and neighboring pixels, while the other considers the relation between sub-pixels. The SPSAM (Mertens et al., 2006) and RBF (Wang et al., 2014a) methods were selected for the former and PSA (Makido et al., 2007) was selected for the latter. For these three benchmark methods, the number of sub-pixels for each class needs to be determined first. The numbers were calculated according to Eq. (10), where uncertainty from the PSF effect exists in the coarse proportions. The SPM results of all five methods are presented in Fig. 7.

Due to the uncertainty in the coarse proportions, the SPM predictions of SPSAM and RBF contain a number of jagged artifacts and the

boundaries of classes are rough. Although PSA is able to enhance the performance and produce a more compact result, the class boundaries are still not smooth and some noisy pixels exist. Different from the three methods, the original HNN method produces a cleaner result and the class boundaries are smoother, although the PSF is not considered. The reason is that the HNN is not absolutely slavish to the coarse proportions, and can remove isolated pixels and produce a compact result by the two spatial clustering functions G1 and G2 (see Eqs. (19) and (17)). However, there are some needle-like artifacts for restoration of roads and trees in the HNN result. Using the proposed method accounting for the PSF effect, the result is more accurate than the original HNN without the PSF method. For example, the prediction of the roads by the proposed method is smoother, and needle-like artifacts are removed. The result of the proposed method is the closest to the reference in Fig. 7(f) amongst all five methods.

Table 4 is the accuracy for the five SPM methods, where two zoom factors, 4 and 8, were tested. Again, the pure pixels were not considered in the accuracy statistics. For both zoom factors, the proposed HNN with PSF method produces the greatest accuracy for all classes, and thus, the largest OA amongst all methods. More specifically, SPSAM, RBF and PSA have very similar accuracies. The three methods produce OA of around 93% for $z = 4$ and 89% for $z = 8$. Compared to the three benchmark methods, the HNN without PSF method is more accurate. For $z = 4$ and 8, the OA is increased by around 3.5% and 3%, respectively. With respect to the proposed HNN with PSF method, the accuracies of roads, trees, buildings and grass are increased by at least 5%, 3%, 3.5% and 4% in comparison with SPSAM, RBF and PSA for $z = 4$, and correspondingly, the OA is increased by over 4%. In addition, with the PSF, the OA is 1% larger than the original HNN method. For $z = 8$, the accuracies of roads, trees and buildings for the proposed method are 3%, 5% and 6% larger than for the HNN without PSF method. Moreover, the OA of the proposed method is 4.6%, 4.9%, 4.8% and 1.9% larger than the SPSAM,

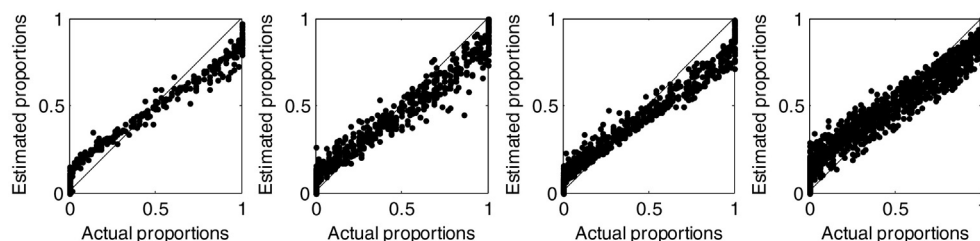


Fig. 6. Relation between the actual proportions and proportions contaminated due to the PSF effect for the land cover map ($z = 8$). From left to right are results for roads, trees, buildings and grass.

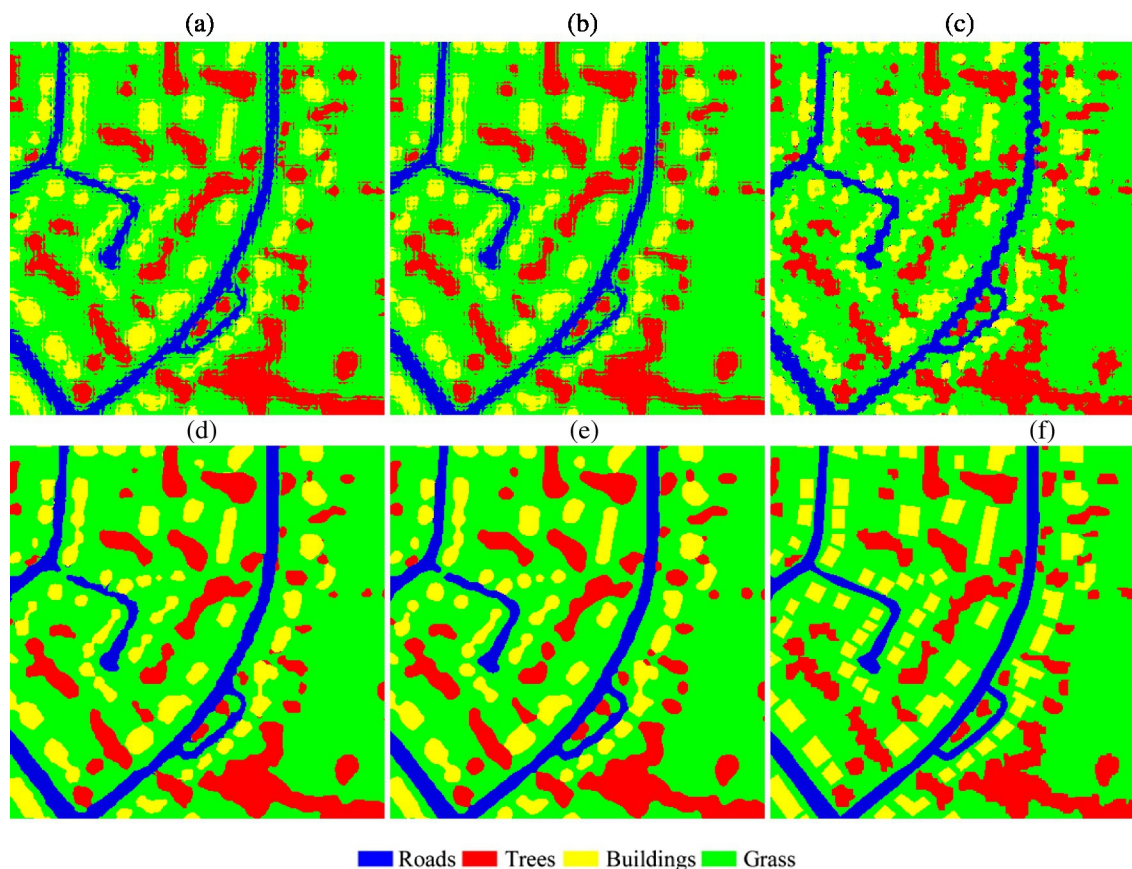


Fig. 7. SPM results of the land cover map with 360 by 360 pixels ($z = 8$). (a) SPSAM (no PSF). (b) RBF (no PSF). (c) PSA (no PSF). (d) HNN (no PSF). (e) The proposed HNN with PSF. (f) Reference.

RBF, PSA and HNN without PSF methods, and the corresponding RREs are 43.29%, 44.70%, 44.29% and 23.57%.

3.3. Experiment on the multispectral image

In this experiment, to control the experimental analysis and ensure the perfect reliability of the reference, a synthesized multispectral image was used. The original multispectral image was acquired by the Landsat-7 Enhanced Thematic Mapper sensor in August 2001 and covers a farmland in the Liaoning Province, China. The spatial resolution is 30 m. The studied area has a spatial size of 240 by 240 pixels and covers mainly four land cover classes (marked as C1–C4). Fig. 8(a) and Fig. 8(b) show the original multispectral image and the corresponding manually digitized reference map. From the reference map, the mean

and variance of each land cover class in the original 30 m Landsat image (bands 1–5 and 7 were considered) were calculated. Referring to Fig. 8(b), the six-band 30 m resolution multispectral image was synthesized based on the random normal distribution and the mean and variance of the classes. Fig. 8(c) shows the synthesized multispectral image. A 240 m coarse image, a spatial resolution comparable to that of medium-spatial-resolution systems such as Moderate Resolution Imaging Spectroradiometer (MODIS), was created by degrading the synthesized 30 m image with a factor of 8, using a Gaussian PSF. Fig. 8(d) shows the 240 m image. With this strategy, the reference land cover map at 30 m is known perfectly for accuracy assessment.

Spectral unmixing was first performed on the 240 m coarse image using the classical linear spectral mixture model. Fig. 9 is the relation between the estimated proportions and actual proportions for the four

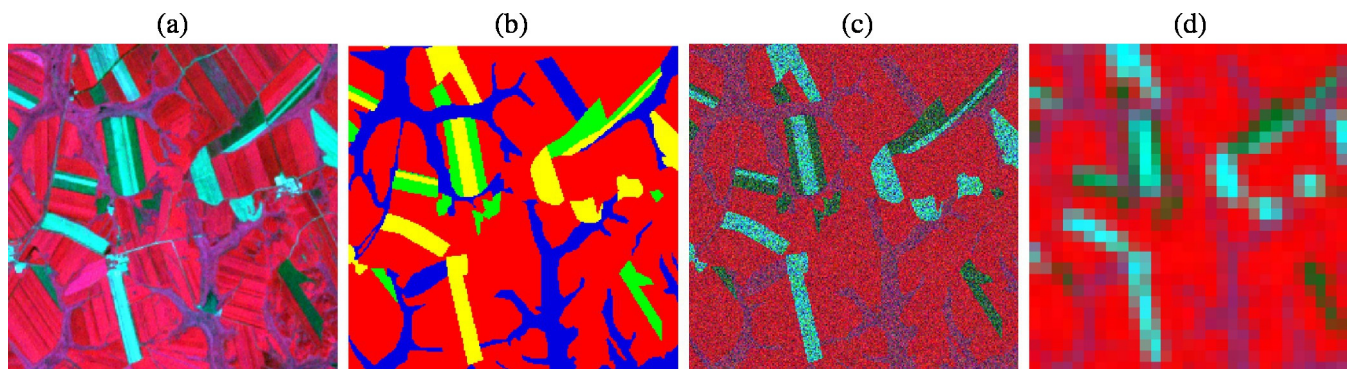


Fig. 8. The multispectral image used for experiment 3. (a) Original 30 m multispectral image (bands 432 as RGB). (b) Reference map drawn manually from (a). (c) Synthesized 30 m multispectral image (bands 432 as RGB). (d) 240 m coarse image produced by degrading (c) with a factor of 8 using a Gaussian PSF.

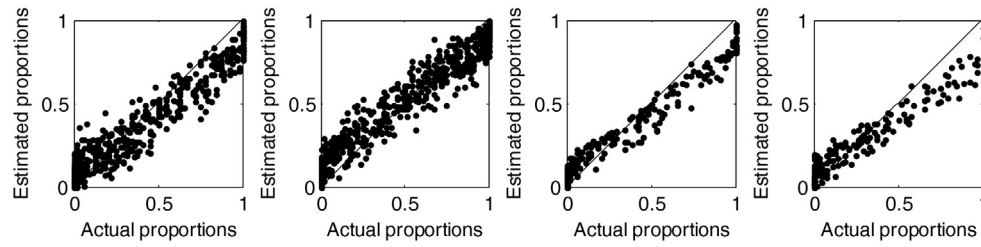


Fig. 9. Relation between the actual proportions and proportions estimated from spectral unmixing for the multispectral image ($z = 8$). From left to right are results for C1–C4.

classes. The errors are visually larger than those in Fig. 6. This is because the errors in proportions in this experiment originate not only from the PSF effect, but also from the spectral unmixing process. This can be supported by the results in Table 5, where the accuracies of the proportions were evaluated using two different references. The convolved proportions were produced by convolving the 30 m land cover map in Fig. 8(b) with the Gaussian PSF. Using the convolved proportions as reference, errors can be observed from only spectral unmixing. As shown in the table, the spectral unmixing errors are particularly large for C1 and C2 (with RMSEs of 0.0418 and 0.0303, respectively). Furthermore, as the PSF introduces additional uncertainty, the accuracies evaluated using the actual proportions as reference are smaller than those for the convolved proportions.

Based on the estimated proportions, SPM was implemented and the results of the five methods are shown in Fig. 10. Failing to account for the PSF, the SPSAM, RBF and PSA predictions are dominated by noisy pixels and spurs on boundaries between classes. As the original HNN method is not completely slavish to the coarse proportions, it can remove the noisy pixels and spurs and produce a smoother result than the SPSAM, RBF and PSA. In Fig. 10(d), however, there are jagged

boundaries, such as for C3 and C4. The prediction is further enhanced by considering the PSF effect in the proposed method. The quantitative assessment in Table 6 suggests that the proposed method produces a larger accuracy for all four classes as well as a larger OA than the other four SPM methods. Note that in this experiment, all pixels were considered in accuracy statistics, including pure pixels. This is because whether a pixel is pure or not is determined by spectral unmixing and we are concerned about the performance of spectral unmixing. The OA of the proposed method is 91.86%, with a gain of more than 5% over SPSAM, RBF and PSA. Compared with the HNN without PSF, the proposed method increases the accuracies of C1 and C4 by 4.5% and 5.5% and the OA by 1.3%. All RREs (in OA) are large, which means that the proposed method reduces the errors obviously. Note that due to the uncertainty in spectral unmixing, the OA of the proposed method is smaller than that for the land cover map in Table 2 ($z = 8$).

4. Discussion

The PSF effect exists ubiquitously in remote sensing images and the pixel signal is contaminated by its neighbors as a result. Existing SPM

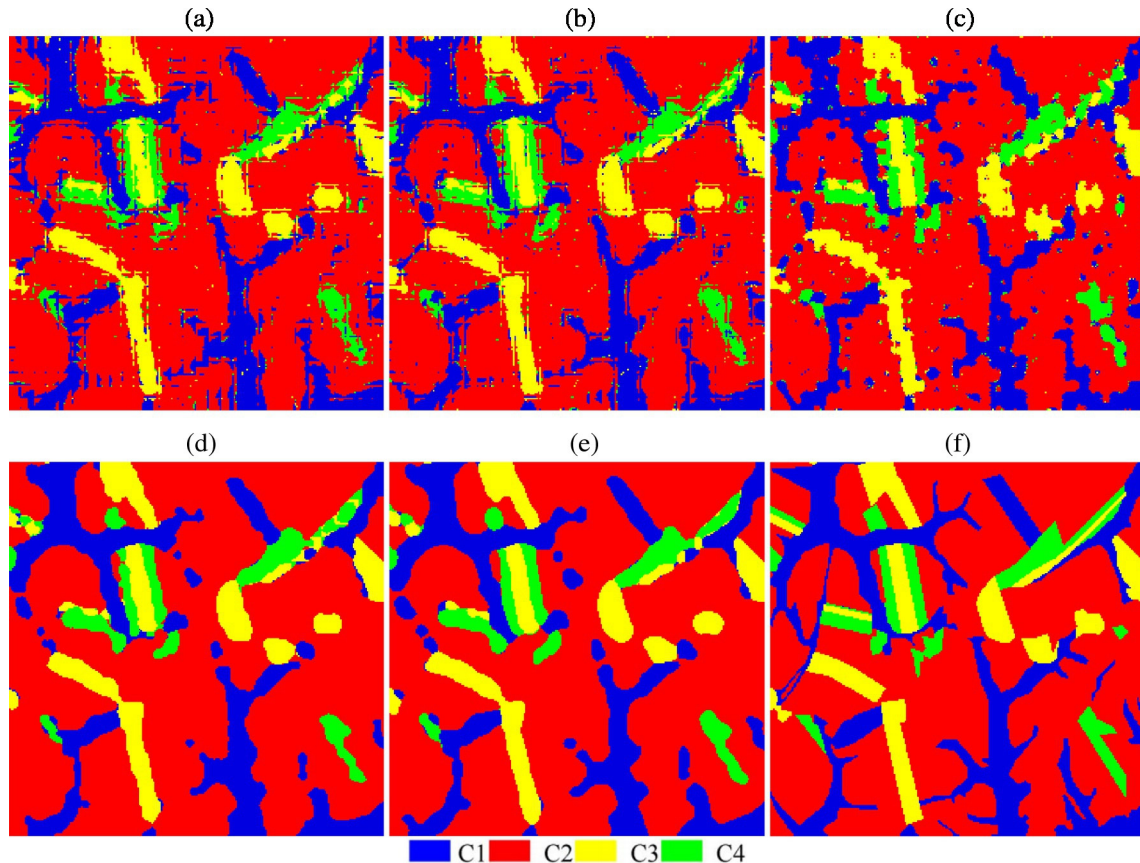


Fig. 10. SPM results of the multispectral image with 240 by 240 pixels ($z = 8$). (a) SPSAM (no PSF). (b) RBF (no PSF). (c) PSA (no PSF). (d) HNN (no PSF). (e) The proposed HNN with PSF. (f) Reference.

methods are generally performed based on the assumption of the ideal square wave filter-based PSF and treat the signal of a coarse pixel as the mean of sub-pixel signals within it. This assumption ignores the effect from neighbors and limits unnecessarily the accuracy of SPM predictions. As shown in the experimental results, the SPSAM, RBF and PSA predictions contain noticeable errors where the PSF is ignored. Note that the performances of the SPSAM, RBF and PSA methods are not as satisfactory as demonstrated in the literature where they were proposed (Makido et al., 2007; Mertens et al., 2006; Wang et al., 2014a). The reason is that in the experimental design in the literature, the coarse images were simulated using the ideal square PSF and, thus, the sub-pixel maps can be satisfactorily reproduced by ignoring the PSF effect.

The proposed SPM approach that considers the PSF effect is developed based on the iterative HNN method. The computing time is the product of the average time consumed in each iteration and the number of required iterations. When considering the PSF effect, more sub-pixels are involved in the convolution process (see Eq. (20)) and more time is needed in each iteration. Moreover, the convergence rate is slower and a larger number of iterations are required. Thus, the proposed method has larger computational cost than the original HNN method without the PSF. In the experiments, the original HNN method is able to converge after 1000 iterations, but the proposed method needs 3000 iterations instead. For SPM of the multispectral image, the running time of the original HNN and the proposed method is 1 and 5 h, respectively. Note that the computational cost of a SPM method is positively related to the spatial size of the input coarse image, number of classes and zoom factor.

This paper considers using HNN to cope with the PSF effect. The solution is identified as modifying the proportion constraint term in the original HNN using a convolution process where contributions from neighboring coarse pixels are accounted for. It would be worthwhile to develop other solutions based on existing SPM methods, such as PSA and the STHSPM methods. For example, in the original PSA method, pixel swapping is allowed only within a coarse pixel. To account for the PSF, the SPM method can be extended by allowing sub-pixel swaps not only within a coarse pixel, but also between coarse pixels. The number of allowable sub-pixel swap between coarse pixels would be a key issue that needs to be addressed. Moreover, it would also be interesting to consider developing artificial intelligence-based methods (e.g., genetic algorithm and PSO, etc.). In such methods, the solutions in the set (called population in genetic algorithm and swarm in PSO) can be updated iteratively according to the fitness values (calculated according to the pre-defined objective) by using related operators (such as crossover and mutation in genetic algorithm and position update in PSO). An optimal solution is expected to be produced after a number of generations. A critical issue for this type of approach would be the definition of the objective, where a constraint term is needed for taking the PSF effect into consideration. Both the prediction accuracy and computational cost will be important indices to identifying an effective method.

Each sensor has its own PSF size. Based on the assumption of a Gaussian filter, some studies were conducted to estimate the PSF size of satellite sensor images. Radoux et al. (2016) estimated the PSF size of Landsat 8 and Sentinel-2 images. It was found that the full-width at half-maximum (FWHM) for Landsat 8 red band is 1.70 pixels (amounting to a width of 0.72 pixel) and ranges from 1.67 to 2.21 pixels (i.e., a width from 0.71 to 0.94 pixel) for Sentinel-2 bands. Campagnolo and Montano (2014) estimated the PSF size of MODIS images at different view zenith angles. The size of the PSF is a critical factor affecting the performance of the proposed method, as displayed in Fig. 4. As the size increases, more neighboring sub-pixels contaminate the center coarse pixel, and the accuracy of the proposed method will decrease correspondingly. However, the advantage of the proposed method over the traditional method (i.e., accuracy gain) is obvious across different PSF sizes, especially for large ones. The encouraging

performance will promote the application of the proposed method for sensors with various PSF sizes.

The main objective of this paper was to find a generic solution to address the PSF effect in SPM and increase the accuracy of SPM predictions. A Gaussian PSF was assumed for convenience in the experimental validation. In reality, the PSF may not be the Gaussian filter, especially for sensors with a rotating/scanning mirror which will ensure that the shape has a directional component. For example, the MODIS sensor PSF was claimed to be triangular in the along-scan direction but rectangular in the along-track direction in Tan et al. (2006). As seen from Eq. (20), however, the proposed method is suitable for any PSF. Thus, in real cases, if the PSF is known or estimated reliably, it can be used readily in the proposed method. This paper provides a first guidance to increase SPM accuracy by considering the PSF effect. It could also help to initiate research on PSF estimation that would ultimately provide the information needed for the use of the proposed method. The PSF estimation mainly includes determination of the specific form of the function and related parameters. This is part of our ongoing research.

The spatial clustering functions G1 and G2 in the HNN make the proposed method more appropriate for SPM in the H-resolution case, where the objects of interest are larger than the pixel size of the input coarse image (Atkinson, 2009). In the L-resolution case where the objects of interest are smaller than the pixel size, alternative prior spatial structure information-based models, such as the semivariogram-based model in Tatem et al. (2002), are more suitable, and should be applied. It would also be worthy of developing models that can adaptively cope with different spatial patterns. Ge et al. (2016) performed a pioneering study for this issue.

Although the proposed method can increase the SPM accuracy, uncertainty still exists. Based on Eq. (6), the ideal SPM solution is identified as the one that when convolved with the PSF, predicts the coarse proportion. There can be multiple solutions satisfying this condition, leading to the perfect coherence constraint. The uncertainty related to this issue can be further reduced by using additional information, such as sub-pixel shifted remote sensing images (Ling et al., 2010; Zhong et al., 2014), panchromatic images (Ardila et al., 2011; Li et al., 2014; Nguyen et al., 2011), high resolution color images (Mahmood et al., 2013), digital elevation models (Huang et al., 2014), time-series images (Wang et al., 2016), segmentation data (Aplin and Atkinson, 2001; Robin et al., 2008) or shape information (Ling et al., 2012). It would be an interesting challenge to design the appropriate model to incorporate such additional information into the proposed method considering the PSF effect for possible enhancement in future research.

5. Conclusion

This paper presents a HNN-based method to account for the PSF effect in SPM and increase the SPM predictions. Based on the recognition of the PSF as a real effect, the coarse proportions are viewed as the convolution of sub-pixels within the local window centered at the coarse pixel, rather than of only the sub-pixels within the coarse pixel. In the proposed HNN-based method, the interim SPM realization is convolved with the PSF and compared with coarse proportions for further updating. The final solution is identified as the one that when convolved with the PSF, is the same as the input coarse proportion. The proposed method is a generic method suitable for any PSF. The effectiveness of the proposed method was validated using three groups of datasets.

Acknowledgment

This work was supported in part by the Research Grants Council of Hong Kong under Grant PolyU 15223015. The authors would also like to thank the handling editor and three anonymous reviewers for their valuable comments which greatly improved the work.

References

- Aplin, P., Atkinson, P.M., 2001. Sub-pixel land cover mapping for per-field classification. *Int. J. Remote Sens.* 22, 2853–2858.
- Ardila, J.P., Tolpekin, V.A., Bijker, W., Stein, A., 2011. Markov-random-field-based super-resolution mapping for identification of urban trees in VHR images. *ISPRS J. Photogramm. Remote Sens.* 66, 762–775.
- Atkinson, P.M., 1997. Mapping sub-pixel boundaries from remotely sensed images. *Innov. GIS* 4, 166–180.
- Atkinson, P.M., 2005. Sub-pixel target mapping from soft-classified, remotely sensed imagery. *Photogramm. Eng. Remote. Sens.* 71, 839–846.
- Atkinson, P.M., 2008. Super-resolution mapping using the two-point histogram and multi-source imagery. *GeoENV VI: Geostatistics for Environmental Applications*, pp. 307–321.
- Atkinson, P.M., 2009. Issues of uncertainty in super-resolution mapping and their implications for the design of an inter-comparison study. *Int. J. Remote Sens.* 30, 5293–5308.
- Bioucas-Dias, J.M., Plaza, A., Dobigeon, N., Parente, M., Du, Q., Gader, P., Chanussot, J., 2012. Hyperspectral unmixing overview: geometrical, statistical and sparse regression-based approaches. *IEEE J. Sel. Top. Appl. Earth Observ. Remote. Sens.* 5, 354–379.
- Boucher, A., Kyriakidis, P.C., 2006. Super-resolution land cover mapping with indicator geostatistics. *Remote Sens. Environ.* 104, 264–282.
- Campagnolo, M.L., Montano, E.L., 2014. Estimation of effective resolution for daily MODIS gridded surface reflectance products. *IEEE Trans. Geosci. Remote Sens.* 52, 5622–5632.
- Chen, Y., Ge, Y., Heuvelink, G.B.M., Hu, J., Jiang, Y., 2015. Hybrid constraints of pure and mixed pixels for soft-then-hard super-resolution mapping with multiple shifted images. *IEEE J. Sel. Top. Appl. Earth Observ. Remote. Sens.* 8, 2040–2052.
- Foody, G.M., Doan, H.T.X., 2007. Variability in soft classification prediction and its implications for sub-pixel scale change detection and super-resolution mapping. *Photogramm. Eng. Remote. Sens.* 73, 923–933.
- Ge, Y., Chen, Y., Li, S., Jiang, Y., 2014. Vectorial boundary-based sub-pixel mapping method for remote-sensing imagery. *Int. J. Remote Sens.* 35, 1756–1768.
- Ge, Y., Chen, Y., Stein, A., Li, S., Hu, J., 2016. Enhanced subpixel mapping with spatial distribution patterns of geographical objects. *IEEE Trans. Geosci. Remote Sens.* 54, 2356–2370.
- Gu, Y., Zhang, Y., Zhang, J., 2008. Integration of spatial-spectral information for resolution enhancement in hyperspectral images. *IEEE Trans. Geosci. Remote Sens.* 46, 1347–1358.
- Heinz, D.C., Chang, C.I., 2001. Fully constrained least squares linear spectral mixture analysis method for material quantification in hyperspectral imagery. *IEEE Trans. Geosci. Remote Sens.* 39, 529–545.
- Huang, C., Townshend, R.G., Liang, S., Kalluri, S.N.V., DeFries, R.S., 2002. Impact of sensor's point spread function on land cover characterization: assessment and deconvolution. *Remote Sens. Environ.* 80, 203–212.
- Huang, C., Chen, Y., Wu, J., 2014. DEM-based modification of pixel-swapping algorithm for enhancing floodplain inundation mapping. *Int. J. Remote Sens.* 35, 365–381.
- Kasetkasem, T., Arora, M.K., Varshney, P.K., 2005. Super-resolution land-cover mapping using a Markov random field based approach. *Remote Sens. Environ.* 96, 302–314.
- Keshava, N., Mustard, J.F., 2002. Spectral unmixing. *IEEE Signal Process. Mag.* 19, 44–57.
- Li, X., Ling, F., Du, Y., Zhang, Y., 2014. Spatially adaptive superresolution land cover mapping with multispectral and panchromatic images. *IEEE Trans. Geosci. Remote Sens.* 52, 2810–2823.
- Li, L., Chen, Y., Xu, T., Liu, R., Shi, K., Huang, C., 2015. Super-resolution mapping of wetland inundation from remote sensing imagery based on integration of back-propagation neural network and genetic algorithm. *Remote Sens. Environ.* 164, 142–154.
- Lin, H., Bo, Y., Wang, J., Jia, X., 2011. Landscape structure based super-resolution mapping from remotely sensed imagery. *Proc. Int. Geosci. Remote Sens. Symp.* 79–82.
- Ling, F., Du, Y., Xiao, F., Xue, H., Wu, S., 2010. Super-resolution land-cover mapping using multiple sub-pixel shifted remotely sensed images. *Int. J. Remote Sens.* 31, 5023–5040.
- Ling, F., Li, X., Xiao, F., Fang, S., Du, Y., 2012. Object-based sub-pixel mapping of buildings incorporating the prior shape information from remotely sensed imagery. *Int. J. Appl. Earth Obs. Geoinf.* 18, 283–292.
- Ling, F., Li, X., Xiao, F., Du, Y., 2014. Superresolution land cover mapping using spatial regularization. *IEEE Trans. Geosci. Remote Sens.* 52, 4424–4439.
- Mahmood, Z., Akhter, M.A., Thoonen, G., Scheunders, P., 2013. Contextual subpixel mapping of hyperspectral images making use of a high resolution color image. *IEEE J. Sel. Top. Appl. Earth Observ. Remote. Sens.* 6, 779–791.
- Makido, Y., Shortridge, A., 2007. Weighting function alternatives for a subpixel allocation model. *Photogramm. Eng. Remote. Sens.* 73, 1233–1240.
- Makido, Y., Shortridge, A., Messina, J.P., 2007. Assessing alternatives for modeling the spatial distribution of multiple land-cover classes at sub-pixel scales. *Photogramm. Eng. Remote. Sens.* 73, 935–943.
- Manslow, J.F., Nixon, M.S., 2002. On the ambiguity induced by a remote sensor's PSF. *Uncertainty in Remote Sensing and GIS*, pp. 37–57.
- Mertens, K.C., Verbeke, L.P.C., Ducheyne, E.I., Wulf, R. De, 2003. Using genetic algorithms in sub-pixel mapping. *Int. J. Remote Sens.* 24, 4241–4247.
- Mertens, K.C., Baset, B.D., Verbeke, L.P.C., Wulf, R. De, 2006. A sub-pixel mapping algorithm based on sub-pixel/pixel spatial attraction models. *Int. J. Remote Sens.* 27, 3293–3310.
- Muad, A.M., Foody, G.M., 2012. Impact of land cover patch size on the accuracy of patch area representation in HNN-based super resolution mapping. *IEEE J. Sel. Top. Appl. Earth Observ. Remote. Sens.* <http://dx.doi.org/10.1109/JSTARS.2012.2191145>.
- Nguyen, M.Q., Atkinson, P.M., Lewis, H.G., 2011. Super-resolution mapping using Hopfield neural network with panchromatic imagery. *Int. J. Remote Sens.* 32, 6149–6176.
- Radoux, J., Chome, G., Jacques, D.C., Waldner, F., Bellemans, N., Matton, N., Lamarche, C., Andrimont, R., Defourny, P., 2016. Sentinel-2's potential for sub-pixel landscape feature detection. *Remote Sens.* 8, 488.
- Robin, A., Hegarat-Masclé, S. Le, Moisan, L., 2008. Unsupervised subpixel classification using coarse-resolution time series and structural information. *IEEE Trans. Geosci. Remote Sens.* 46, 1359–1374.
- Schowengerdt, R.A., 1997. *Remote Sensing: Models and Methods for Image Processing*. Academic Press, San Diego.
- Shen, Z., Qi, J., Wang, K., 2009. Modification of pixel-swapping algorithm with initialization from a sub-pixel/pixel spatial attraction model. *Photogramm. Eng. Remote. Sens.* 75, 557–567.
- Su, Y.F., Foody, G.M., Muad, A.M., Cheng, K.S., 2012. Combining pixel swapping and contouring methods to enhance super-resolution mapping. *IEEE J. Sel. Top. Appl. Earth Observ. Remote. Sens.* 5, 1428–1437.
- Tan, B., Woodcock, C.E., Hu, J., Zhang, P., Ozdogan, M., Huang, D., Yang, W., Knyazikhin, Y., Myneni, R.B., 2006. The impact of gridding artifacts on the local spatial properties of MODIS data: implications for validation, compositing, and band-to-band registration across resolutions. *Remote Sens. Environ.* 105, 98–114.
- Tatem, A.J., Lewis, H.G., Atkinson, P.M., Nixon, M.S., 2001. Super-resolution target identification from remotely sensed images using a Hopfield neural network. *IEEE Trans. Geosci. Remote Sens.* 39, 781–796.
- Tatem, A.J., Lewis, H.G., Atkinson, P.M., Nixon, M.S., 2002. Super-resolution land cover pattern prediction using a Hopfield neural network. *Remote Sens. Environ.* 79, 1–14.
- Tolpekin, V.A., Stein, A., 2009. Quantification of the effects of land-cover-class spectral separability on the accuracy of Markov-random-field based superresolution mapping. *IEEE Trans. Geosci. Remote Sens.* 47, 3283–3297.
- Tong, X., Xu, X., Plaza, A., Xie, H., Pan, H., Cao, W., Lv, D., 2016. A new genetic method for subpixel mapping using hyperspectral images. *IEEE J. Sel. Top. Appl. Earth Observ. Remote. Sens.* 9, 4480–4491.
- Townshend, R.G., Huang, C., Kalluri, S.N.V., Defries, R.S., Liang, S., 2000. Beware of per-pixel characterization of land cover. *Int. J. Remote Sens.* 21, 839–843.
- Van der Meer, F.D., 2012. Remote-sensing image analysis and geostatistics. *Int. J. Remote Sens.* vol. 33 (18), 5644–5676.
- Verhoeve, J., Wulf, R. De, 2002. Land-cover mapping at sub-pixel scales using linear optimization techniques. *Remote Sens. Environ.* 79, 96–104.
- Villa, A., Chanussot, J., Benediktsson, J.A., Jutten, C., 2011. Spectral unmixing for the classification of hyperspectral images at a finer spatial resolution. *IEEE J. Sel. Top. Signal Process.* 5, 521–533.
- Wang, Q., Wang, L., Liu, D., 2012. Particle swarm optimization-based sub-pixel mapping for remote-sensing imagery. *Int. J. Remote Sens.* 33, 6480–6496.
- Wang, Q., Shi, W., Atkinson, P.M., 2014a. Sub-pixel mapping of remote sensing images based on radial basis function interpolation. *ISPRS J. Photogramm. Remote Sens.* 92, 1–15.
- Wang, Q., Shi, W., Wang, L., 2014b. Allocating classes for soft-then-hard subpixel mapping algorithms in units of class. *IEEE Trans. Geosci. Remote Sens.* 52, 2940–2959.
- Wang, Q., Shi, W., Atkinson, P.M., Zhao, Y., 2015. Downscaling MODIS images with area-to-point regression kriging. *Remote Sens. Environ.* 166, 191–204.
- Wang, Q., Shi, W., Atkinson, P.M., 2016. Spatial-temporal sub-pixel mapping of time-series images. *IEEE Trans. Geosci. Remote Sens.* 54, 5397–5411.
- Wenny, B.N., Helder, D., Hong, J., Leigh, L., Thome, K.J., Reuter, D., 2015. Pre- and post-launch spatial quality of the Landsat 8 Thermal Infrared Sensor. *Remote Sens.* 7, 1962–1980.
- Xu, Y., Huang, B., 2014. A spatio-temporal pixel-swapping algorithm for subpixel land cover mapping. *IEEE Geosci. Remote Sens. Lett.* 11, 474–478.
- Xu, X., Zhong, Y., Zhang, L., 2014. A sub-pixel mapping method based on an attraction model for multiple shifted remotely sensed images. *Neurocomputing* 134, 79–91.
- Zhang, L., Wu, K., Zhong, Y., Li, P., 2008. A new sub-pixel mapping algorithm based on a BP neural network with an observation model. *Neurocomputing* 71, 2046–2054.
- Zhang, Y., Du, Y., Ling, F., Fang, S., Li, X., 2014. Example-based super-resolution land cover mapping using support vector regression. *IEEE J. Sel. Top. Appl. Earth Observ. Remote. Sens.* 7, 1271–1283.
- Zhang, Y., Du, Y., Ling, F., Li, X., 2015. Improvement of the example-regression-based super-resolution land cover mapping algorithm. *IEEE Geosci. Remote Sens. Lett.* 12, 1740–1744.
- Zhong, Y., Wu, Y., Zhang, L., Xu, X., 2014. Adaptive MAP sub-pixel mapping model based on regularization curve for multiple shifted hyperspectral imagery. *ISPRS J. Photogramm. Remote Sens.* 96, 134–148.
- Zhong, Y., Wu, Y., Xu, X., Zhang, L., 2015. An adaptive subpixel mapping method based on MAP model and class determination strategy for hyperspectral remote sensing imagery. *IEEE Trans. Geosci. Remote Sens.* 53, 1411–1426.